

# Determination of the neutron skin thickness from interaction cross section and charge-changing cross section for B, C, N, O, F isotopes

Xiu-Fang Li<sup>1,2</sup> · De-Qing Fang<sup>1</sup> · Yu-Gang Ma<sup>1</sup>

Received: 13 March 2016 / Revised: 21 March 2016 / Accepted: 28 March 2016 / Published online: 14 May 2016  
© Shanghai Institute of Applied Physics, Chinese Academy of Sciences, Chinese Nuclear Society, Science Press China and Springer Science+Business Media Singapore 2016

**Abstract** The effective neutron and proton root-mean-square radius of stable and unstable nuclei ( $^{12-15,17}\text{B}$ ,  $^{12-20}\text{C}$ ,  $^{14-21}\text{N}$ ,  $^{16-24}\text{O}$  and  $^{18-21,23-26}\text{F}$ ) were deduced from the charge-changing cross section,  $\sigma_{cc}$ , and the interaction cross sections,  $\sigma_I$ , by using a statistical abrasion–ablation model calculation. The extracted proton radii are in good agreement with the data from the Atomic Data and Nuclear Data Tables within the errors. Furthermore, we can observe that the neutron skin thickness increases monotonously with the increasing neutron number in these isotopes, which is consistent with the systematical trend of theoretical calculations.

**Keywords** Unstable nuclei · Statistical abrasion–ablation model · Neutron skin thickness

## 1 Introduction

Researches on proton and neutron density distributions in nuclei are very important in nuclear physics for the study of neutron skin [1] or neutron halo structure [2]. Usually, at the

nuclear surface, an excess of neutrons is qualitatively described as the neutron skin. The neutron halo is defined as a long tail of neutron density plus the excess. With the improvement of measuring methods and the high experimental precision of instruments, the uncertainties of the nuclear charge radius measured by muon–nucleus scattering and elastic electron–nucleus experiments are smaller than 1 % [3, 4]. This allows for the deduction of the proton rms radius ( $R_p = \langle r_p^2 \rangle^{1/2}$ ) precisely. In contrast, the neutron density distribution in nuclei is very difficult to measure directly. Actually, we lack accurate methods to determine the rms radius of the neutron density ( $R_n = \langle r_n^2 \rangle^{1/2}$ ). This indicates that the neutron skin thickness has no precise value either, which is defined as the neutron–proton rms radius difference,  $\Delta R_{np} = R_n - R_p$  [5, 6].

Since the mid-1950s, many discussions about the existence of a neutron skin in stable nuclei have occurred. At first, there was no evidence for a thick neutron skin in stable nuclei, even though many of stable nuclei have a large neutron excess (N–Z). However, Tanihata et al. measured the neutron skin thickness of  $^8\text{He}$  to be 0.9 fm [7]. A similar observation was made by Suzuki et al. for the neutron skin thickness in Na isotopes [8]. Therefore, further investigation on the neutron skin is important to understand the ground-state properties of nuclei, which are far away from the  $\beta$  stability line [9–11]. On the other hand, the research about the neutron skin has an important effect for nuclear structure and nuclear symmetry energy [12–14]. As is well known, the nuclear matter radii of light nuclei are determined by measurements of the interaction cross sections ( $\sigma_I$ ) [15–19] or the reaction cross sections [20, 21]. Although these measurements can give the matter radii, the neutron and the proton radii are still lacking and need to be measured separately.

---

This work was supported by the Major State Basic Research Development Program of China (No. 2013CB834405) and the National Natural Science Foundation of China (Nos. 11421505, 11475244 and 11175231).

---

✉ De-Qing Fang  
dqfang@sinap.ac.cn

<sup>1</sup> Shanghai Institute of Applied Physics, Chinese Academy of Sciences, Shanghai 201800, China

<sup>2</sup> University of Chinese Academy of Sciences, Beijing 100049, China

In Ref. [22], it is proposed to extract the proton rms radii  $R_p$  from charge-changing cross sections ( $\sigma_{cc}$ ). If the nuclear matter rms radii,  $R_m$ , are determined from interaction cross-section data, the neutron rms radii,  $R_n$ , can be deduced by using the relationship between  $R_p$ ,  $R_n$  and  $R_m$ . In this work, systematic calculations of proton and neutron rms radii combined with the data of interaction cross sections and charge-changing cross sections for B, C, N, O, and F isotopes have been done by a statistical abrasion–ablation (SAA) model [23–26]. The interaction cross section,  $\sigma_I$ , and charge-changing cross section,  $\sigma_{cc}$ , of  $^{12-15,17}\text{B}$ ,  $^{12-20}\text{C}$ ,  $^{14-21}\text{N}$ ,  $^{16-24}\text{O}$ , and  $^{18-21,23-26}\text{F}$  on a carbon target have been measured at high energies [22, 27]. The neutron skin thicknesses for these isotopes are deduced for the first time by reproducing the measured  $\sigma_I$  and  $\sigma_{cc}$ . Within the errors, most of the extracted neutron skin thickness data are in agreement with the systematics.

This paper is organized as follows: A brief introduction about the statistical abrasion–ablation (SAA) model and the form of density distribution is given in Sect. 2. In Sect. 3, we compare the extracted  $R_p$  from  $\sigma_{cc}$  with the experimental data measured by other methods. Then, we continue to deduce  $R_n$  by the SAA model. Finally,  $\Delta R_{np}$  is obtained from the difference of the neutron and proton rms radii. The conclusions are presented in Sect. 4.

## 2 Model description

### 2.1 Statistical abrasion–ablation (SAA) model

A statistical abrasion–ablation model is presented by Brohm et al. [23–26] to describe high-energy peripheral nuclear reactions. The model uses the individual nucleon–nucleon collisions happening in the overlap zone of the colliding nuclei to describe the collision process and calculate the abraded neutron and proton numbers. The neutron and proton density distributions in the projectile are treated separately in the SAA model, which allows us to study the dependence of fragmentation cross sections on neutron and proton densities, respectively. The SAA model has been modified to satisfy the reaction in low energy [28].

The total reaction cross section  $\sigma_R$  in SAA is calculated by using the Glauber method. It is described by the following equations:

$$\sigma_R = 2\pi \int b[1 - T(b)]db, \tag{1}$$

$$T(b) = \exp \left[ - \sum_{ij} \sigma_{ij} \int \rho_z^{\text{targ}}(s) \rho_z^{\text{proj}}(|b - s|) ds \right], \tag{2}$$

where  $b$  stands for the impact parameter,  $T(b)$  is the transmission function,  $\sigma_{ij}$  denotes the nucleon–nucleon

collision cross sections, and  $\rho_z^{\text{targ}}$  or  $\rho_z^{\text{proj}}$  is the  $z$ -integrated density distribution of the target or projectile.

Following Refs. [29, 30], we take  $T = T^p T^n$  by the following equations:

$$T^p(b) = \exp \left[ - \left( \sigma_{pp} \int \rho_p^{\text{targ}} \rho_p^{\text{proj}} + \sigma_{np} \int \rho_n^{\text{targ}} \rho_p^{\text{proj}} \right) \right], \tag{3}$$

$$T^n(b) = \exp \left[ - \left( \sigma_{pn} \int \rho_p^{\text{targ}} \rho_n^{\text{proj}} + \sigma_{nn} \int \rho_n^{\text{targ}} \rho_n^{\text{proj}} \right) \right], \tag{4}$$

where  $T^p$  is only the proton contribution of the projectile and  $T^n$  is only the neutron contribution of the projectile. Therefore, two pure cross sections and a cross term cross section can be defined:

$$\tilde{\sigma}_{cc} = 2\pi \int b[1 - T^p(b)]db, \tag{5}$$

$$\tilde{\sigma}_{-nx} = 2\pi \int b[1 - T^n(b)]db, \tag{6}$$

$$\sigma_{\text{cross}} = -2\pi \int b[1 - T^p(b)][1 - T^n(b)]db. \tag{7}$$

Obviously,  $\sigma_R = \tilde{\sigma}_{cc} + \tilde{\sigma}_{-nx} + \sigma_{\text{cross}}$ . Since inelastic scattering can be neglected at high energies, the reaction cross section is approximate to the interaction cross section, namely  $\sigma_R \approx \sigma_I$ . Moreover, the charge-changing cross section,  $\sigma_{cc}$ , plus the neutron-removal cross section,  $\sigma_{-nx}$ , is equal to the interaction cross section. Then, the reaction cross section is  $\sigma_R \approx \sigma_{cc} + \sigma_{-nx}$ . The charge-changing cross section,  $\sigma_{cc}$ , is not only made up of projectile-proton contributions, but also the cross term,  $\sigma_{\text{cross}}$ . As shown in Ref. [29], it can be calculated by the following equation,

$$\sigma_{cc} = 2\pi \int b[1 - T^p(b)]\varepsilon(E)db, \tag{8}$$

where  $\varepsilon(E)$  is the correction factor, which is defined as  $\sigma_{cc}/\tilde{\sigma}_{cc}$ , namely the ratio of the experimental  $\sigma_{cc}$  data and calculated  $\tilde{\sigma}_{cc}$  values, as shown in Fig. 1.

In Ref. [29], the relation of the correction factor with the energy ( $\varepsilon(E)$ ) is fitted by a linear function, while the energy changes from 100 to 600 MeV/nucleon, as shown by the dashed line in Fig. 1. The data represented by solid circles are from Ref. [29], and the solid squares are from Ref. [31]. However, the energies of the  $\sigma_{cc}$  for B, C, N, O, and F isotopes in our work are close to 1000 MeV/nucleon. So it is necessary to get the correction factor,  $\varepsilon(E)$ , at high energies. From Fig. 1, we can see that if the energy in the linear correction factor,  $\varepsilon(E)$ , is directly extended to high energy, such as 800 MeV/nucleon or 1200 MeV/nucleon, there is a big deviation with the data. Considering the weak energy dependence of the cross sections for energies above

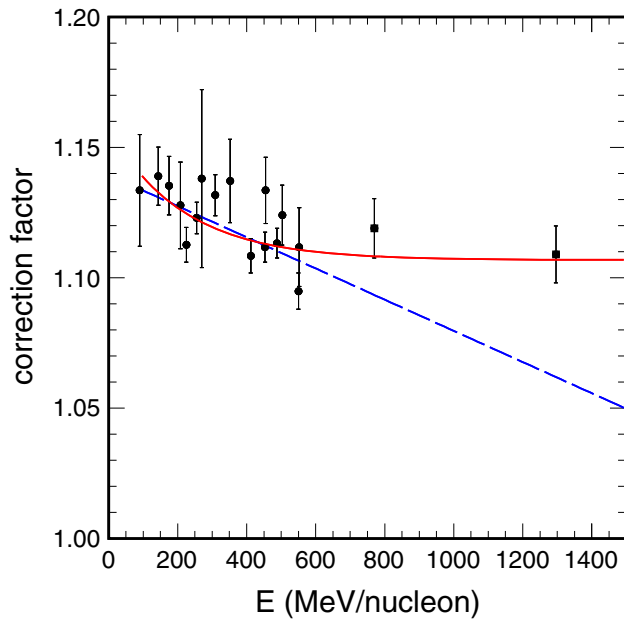


**Fig. 1** (Color online) Energy dependence relation of the correction factor  $\varepsilon(E)$ . The data represented by *solid circles* are from Ref. [29] and *solid square* from Ref. [31]. The *dashed line* is from a linear fitting for the energy range 100–600 MeV/nucleon from Yamaguchi et al. and the *solid line* from an exponential fitting for the energy range 100–1500 MeV/nucleon

600 MeV/nucleon, it is more reasonable to fit energy dependence of the correction factor,  $\varepsilon(E)$ , by an exponential function. The fitted result is shown by the solid line. The expression of the exponential function is as follows:

$$\varepsilon(E) = 1.107 + 0.01191 \times \exp(1.444 - 0.004623E). \quad (9)$$

## 2.2 Density distribution

For the proton and neutron density distribution in the projectile, we use the two-parameter Fermi-type function. According to the droplet model [25, 26], the density,  $\rho_i(r)$ , at a distance  $r$  in the SAA model is given by

$$\rho_i(r) = \frac{\rho_i^0}{1 + \exp\left(\frac{r-C_i}{t_i/4.4}\right)}, \quad i = n, p, \quad (10)$$

$$C_i = R_i^{\text{sur}}[1 - (0.413t_i/R_i^{\text{sur}})^2], \quad i = n, p, \quad (11)$$

$$R_i^{\text{sur}} = R_{0i} + (Z/A)D, \quad i = n, p, \quad (12)$$

$$D = \frac{2}{3}R_{0i} \left[ \frac{A - 2Z}{A} - \delta \right] / B_s, \quad i = n, p, \quad (13)$$

where  $\rho_i^0$  denotes the normalization parameter of the neutrons' ( $i = n$ ) or protons' ( $i = p$ ) density distribution;  $t_i$  stands for the diffuseness parameter;  $C_i$  is the neutron or proton half-density radius;  $R_i^{\text{sur}}$  is called the equivalent

neutron or proton sharp-surface radius; and  $R_{0i}$  is the separate effective neutron or proton sharp radii.

Here, we introduce the neutron and proton radii constant,  $r_{0i}$ , instead of the former matter radii constant,  $r_0$ , to the  $R_{0i}$ , namely,

$$R_{0i} = r_{0i}A^{1/3}(1 + \epsilon), \quad i = n, p. \quad (14)$$

Parameters  $\delta$ ,  $B_s$ , and  $\epsilon$  are determined by Ref. [26]. As for the matter radii constant, we assume the relationship  $r_0^2 = \frac{N}{A}r_{0n}^2 + \frac{Z}{A}r_{0p}^2$ . From the perspective of calculation accuracy and convenience, we chose directly to change the neutron radii constant,  $r_{0n}$ , instead of  $r_0$  to reproduce  $\sigma_1$ . Now we can use the  $\sigma_{cc}$  to get  $r_{0p}$  and use  $\sigma_1$  to get  $r_{0n}$ . The calculation details are described in the following.

## 3 Calculation and discussion

The  $\sigma_{cc}$  for  $^{12-15,17}\text{B}$ ,  $^{12-20}\text{C}$ ,  $^{14-21}\text{N}$ ,  $^{16-24}\text{O}$ , and  $^{18-21,23-26}\text{F}$  was measured by Chulkov et al. at  $930 \pm 44$  MeV/u on a carbon target [27]. A summary for the interaction cross section  $\sigma_1$  on Be, C, and Al targets has been presented by Ozawa et al. [22]. For consistency, only the  $\sigma_{cc}$  and  $\sigma_1$  data on the C target are used.

### 3.1 The proton rms radii

From Eq. (8), the charge-changing cross section is mainly determined by the proton density distribution of projectile  $\rho_p$  and  $\varepsilon(E)$  from Eq. (9). However, from Eq. (10),  $\rho_p$  is mainly determined by the proton radius constant,  $r_{0p}$ .

In our work, by adjusting the input parameter  $r_{0p}$ , the experimental  $\sigma_{cc}$  will be reproduced. Once the  $r_{0p}$  is fixed, we can get the proton rms radius,  $R_p$ , from  $\rho_p$ .

The extracted proton rms radii are compared with the data given by the Atomic Data and Nuclear Data Tables [32], as shown in Fig. 2.

In Fig. 2, the data represented by solid squares are determined from the updated charge radii,  $R_c$ , of the Atomic Data and Nuclear Data Tables in 2013 [32]. Using the relation  $R_p^2 = R_c^2 - 0.64$ , we can get the corresponding  $R_p$  from the Atomic Data and Nuclear Data Tables. The open circles represent the extracted  $R_p$  values from  $\sigma_{cc}$  using the SAA model. From Fig. 2, we can see that the calculations using the SAA model are nearly consistent with data from the Atomic Data and Nuclear Data Tables within the error bars.

### 3.2 The neutron rms radii

Due to the limited  $R_c$  of B, C, N, O, and F isotopes from the Atomic Data and Nuclear Data Tables, only a few

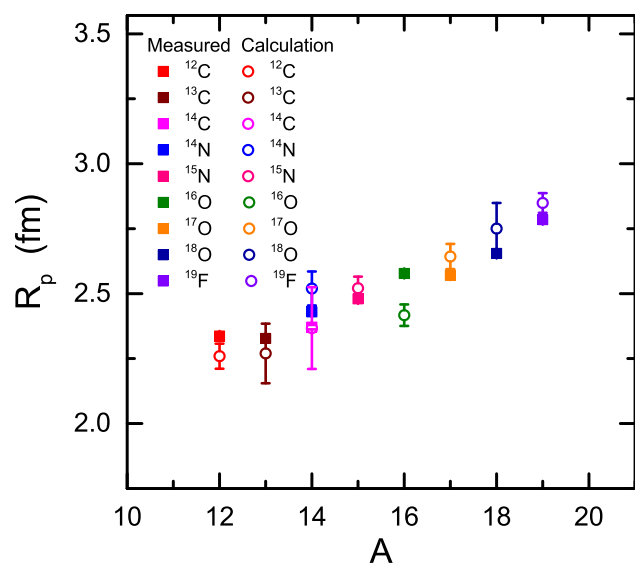


**Fig. 2** (Color online) A comparison of the rms proton radius  $R_p$  for nuclei  $^{12}\text{C}$ ,  $^{13}\text{C}$ ,  $^{14}\text{C}$ ,  $^{14}\text{N}$ ,  $^{15}\text{N}$ ,  $^{16}\text{O}$ ,  $^{17}\text{O}$ ,  $^{18}\text{O}$ , and  $^{19}\text{F}$ . The *solid squares* are measured data taken from the Atomic Data and Nuclear Data Tables [32], and the *open circles* are the calculated results by SAA model

proton radii are compared in Fig. 2. The  $R_p$  of more isotopes, including  $^{12-15,17}\text{B}$ ,  $^{12-20}\text{C}$ ,  $^{14-21}\text{N}$ ,  $^{16-24}\text{O}$ , and  $^{18-21,23-26}\text{F}$ , is deduced using the same method.

After the proton radii constant,  $r_{0p}$ , is fixed, the neutron radii constant,  $r_{0n}$ , is adjusted to reproduce the experimental  $\sigma_I$  data. In the SAA model, the  $\sigma_{cc}$  is mainly determined by the proton radii constant,  $r_{0p}$ . Therefore, when the  $r_{0p}$  is fixed, even though  $r_{0n}$  is changeable in the process of fitting  $\sigma_I$ , the  $\sigma_{cc}$  value has little change, less than 0.7 %. The values of the neutron and proton rms radii extracted by the SAA model are shown in Fig. 3.

In Fig. 3, the data represented by squares are  $R_n$  and circles are  $R_p$ . The proton rms radii of  $^{12}\text{B}$  have a large error because the measured  $\sigma_{cc}$  for  $^{12}\text{B}$  have a large error. And the neutron rms radii of  $^{16}\text{N}$  has a large error because the measured  $\sigma_I$  for  $^{16}\text{N}$  has a large error. On the other hand, we can see that with the growth of the mass number in each isotope chain, the neutron rms radii increase slowly, while the corresponding proton rms radii are almost constant with the mass number increasing.

When the neutron number nearly equals to the proton number, namely the neutron excess ( $N-Z$ ) is close to zero, the neutron–proton rms radius difference becomes small, which indicates that proton and neutron density distributions in the stable nuclei are almost the same. As the ( $N-Z$ ) increases, the difference between  $R_n$  and  $R_p$  becomes large. Combining the analysis above, it is illustrated that neutron excess influences  $R_n$  more than  $R_p$ .

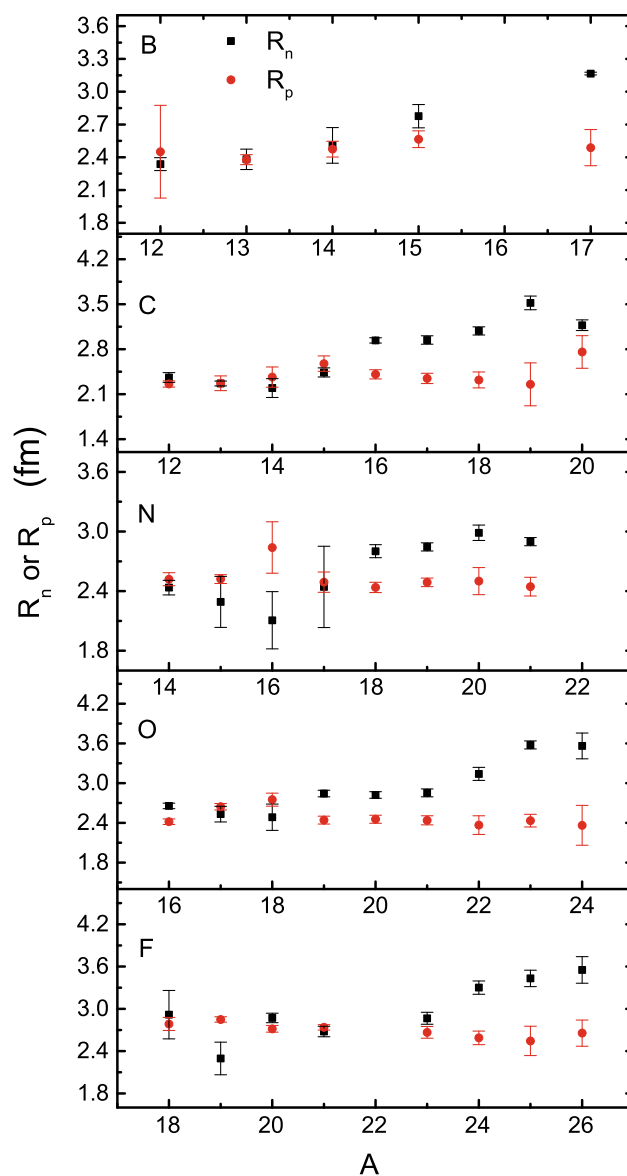


**Fig. 3** (Color online) The rms neutron radius  $R_n$  and proton radii  $R_p$  calculated by SAA for the nuclei  $^{12-15,17}\text{B}$ ,  $^{12-20}\text{C}$ ,  $^{14-21}\text{N}$ ,  $^{16-24}\text{O}$  and  $^{18-21,23-26}\text{F}$ .  $R_n$  is represented by *squares* and  $R_p$  by *circles*

### 3.3 The neutron skin thickness

In Fig. 4, the neutron skin thickness determined from the difference between the neutron and proton rms radii is plotted with the separation energy difference between proton and neutron ( $S_p - S_n$ ). We can see that  $\Delta R_{np}$  of B, C, N, O, and F is strongly connected with ( $S_p - S_n$ ), i.e., the neutron skin thickness increases with an increase in  $S_p - S_n$ . Such a correlation has been predicted by Tanihata et al. using the RMF model [7] and is shown by the shadow area in Fig. 4. The neutron skin thicknesses determined by

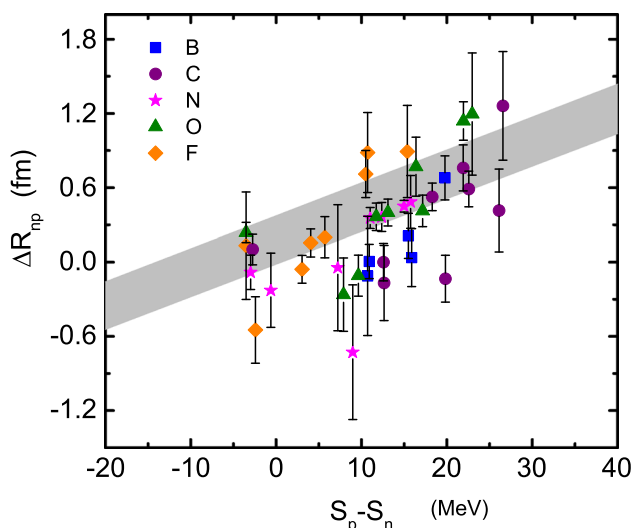


**Fig. 4** (Color online) The relation between the proton and neutron separation energy difference and the neutron skin thickness. The *shadow area* shows the calculated correlation for various isotopes, ranging from helium up to lead [7]

the method presented in this work agree well with the theoretical systematics.

#### 4 Conclusion

In summary, we have extracted the neutron rms radii,  $R_n$ , and proton rms radii,  $R_p$ , of  $^{12-15,17}\text{B}$ ,  $^{12-20}\text{C}$ ,  $^{14-21}\text{N}$ ,  $^{16-24}\text{O}$ , and  $^{18-21,23-26}\text{F}$  from interaction cross sections and charge-changing cross sections with the SAA model. The extracted proton radii with the SAA model are in good agreement with the data. The neutron radii,  $R_n$ , increases faster than  $R_p$ , which stays almost constant. Furthermore, we have shown an increase in the neutron skin  $\Delta R_{np}$  in the neutron-rich isotopes of B, C, N, O, and F. The extracted results are consistent with the systematics. It indicates the feasibility of the method for extracting proton and neutron radii from  $\sigma_{cc}$  and  $\sigma_I$  data.

#### References

1. D.Q. Fang, Y.G. Ma et al., Neutron removal cross section as a measure of neutron skin. *Phys. Rev. C* **81**, 047603 (2010). doi:[10.1103/PhysRevC.81.047603](https://doi.org/10.1103/PhysRevC.81.047603)
2. D.Q. Fang et al., One-neutron halo structure in  $^{15}\text{C}$ . *Phys. Rev. C* **69**, 034613 (2004). doi:[10.1103/PhysRevC.69.034613](https://doi.org/10.1103/PhysRevC.69.034613)
3. G. Fricke, C. Bernhardt et al., Nuclear ground state charge radii from electromagnetic interactions. *At. Data Nucl. Data Tables* **60**, 177 (1995). doi:[10.1006/adnd.1995.1007](https://doi.org/10.1006/adnd.1995.1007)
4. I. Angeli, A consistent set of nuclear rms charge radii: properties of the radius surface  $R(N, Z)$ . *At. Data Nucl. Data Tables* **87**, 185 (2004). doi:[10.1016/j.adt.2004.04.002](https://doi.org/10.1016/j.adt.2004.04.002)

5. M. Centelles, X. Roca-Maza, X. Vinas, M. Warda, Origin of the neutron skin thickness of  $^{208}\text{Pb}$  in nuclear mean field-models. *Phys. Rev. C* **82**, 054314 (2010). doi:[10.1103/PhysRevC.82.054314](https://doi.org/10.1103/PhysRevC.82.054314)
6. M. Warad, X. Vinas, M. Centelles, Analysis of bulk and surface contributions in the neutron skin of nuclei. *Phys. Rev. C* **81**, 054309 (2010). doi:[10.1103/PhysRevC.81.054309](https://doi.org/10.1103/PhysRevC.81.054309)
7. I. Tanihata, D. Hirata et al., Revelation of thick neutron skins in nuclei. *Phys. Lett. B* **289**, 261 (1992). doi:[10.1016/0370-2693\(92\)91216-V](https://doi.org/10.1016/0370-2693(92)91216-V)
8. T. Suzuki, H. Geissel et al., Neutron skin of Na isotopes studied via their interaction cross sections. *Phys. Rev. L* **75**, 3241 (1995). doi:[10.1103/PhysRevLett.75.3241](https://doi.org/10.1103/PhysRevLett.75.3241)
9. M. Yu, S.J. Duan et al., A nuclear density probe: isobaric yield ratio difference. *Nucl. Sci. Tech.* **26**, S20503 (2015). doi:[10.13538/j.1001-8042/nst.26.S20503](https://doi.org/10.13538/j.1001-8042/nst.26.S20503)
10. Z.T. Dai, D.Q. Fang, Y.G. Ma et al., Triton/ $^3\text{He}$  ratio as an observable for neutron-skin thickness. *Phys. Rev. C* **89**, 014613 (2014). doi:[10.1103/PhysRevC.89.014613](https://doi.org/10.1103/PhysRevC.89.014613)
11. Z.T. Dai, D.Q. Fang, Y.G. Ma et al., Effect of neutron skin thickness on projectile fragmentation. *Phys. Rev. C* **91**, 034618 (2015). doi:[10.1103/PhysRevC.91.034618](https://doi.org/10.1103/PhysRevC.91.034618)
12. X.Q. Liu et al., Symmetry energy extraction from primary fragments in intermediate heavy-ion collisions. *Nucl. Sci. Tech.* **26**, S20508 (2015). doi:[10.13538/j.1001-8042/nst.26.S20508](https://doi.org/10.13538/j.1001-8042/nst.26.S20508)
13. D.Q. Fang et al., Examining the exotic structure of the proton-rich nucleus  $^{23}\text{Al}$ . *Phys. Rev. C* **76**, 031601 (2007). doi:[10.1103/PhysRevC.76.031601](https://doi.org/10.1103/PhysRevC.76.031601)
14. Y. Kanada-En'yo et al., Cluster structures in stable and unstable nuclei. *Nucl. Sci. Tech.* **26**, S20501 (2015). doi:[10.13538/j.1001-8042/nst.26.S20501](https://doi.org/10.13538/j.1001-8042/nst.26.S20501)
15. I. Tanihata et al., Measurements of interaction cross sections and radii of He isotopes. *Phys. Lett. B* **160**, 380 (1985). doi:[10.1016/0370-2693\(85\)90005-X](https://doi.org/10.1016/0370-2693(85)90005-X)
16. I. Tanihata, H. Hamagaki et al., Measurements of interaction cross sections and nuclear radii in the light p-shell region. *Phys. Rev. Lett.* **55**, 2676 (1985). doi:[10.1103/PhysRevLett.55.2676](https://doi.org/10.1103/PhysRevLett.55.2676)
17. I. Tanihata, T. Kobayashi et al., Measurement of interaction cross sections using isotope beams of Be and B and isospin dependence of the nuclear radii. *Phys. Lett. B* **206**, 592 (1988). doi:[10.1016/0370-2693\(88\)90702-2](https://doi.org/10.1016/0370-2693(88)90702-2)
18. R. Qiu, Y.Y. Liu et al., Measurement and validation of the cross section in the FLUKA code for the production of  $^{63}\text{Zn}$  and  $^{65}\text{Zn}$  in Cu targets for low-energy proton accelerators. *Nucl. Sci. Tech.* **25**, S010202 (2014). doi:[10.13538/j.1001-8042/nst.25.S010202](https://doi.org/10.13538/j.1001-8042/nst.25.S010202)
19. D.Q. Fang, W.Q. Shen, J. Feng et al., Measurements of total reaction cross sections for some light nuclei at intermediate energies. *Phys. Rev. C* **61**, 064311 (2000). doi:[10.1103/PhysRevC.61.064311](https://doi.org/10.1103/PhysRevC.61.064311)
20. M. Fukuda et al., Neutron halo in  $^{11}\text{Be}$  studied via reaction cross sections. *Phys. Lett. B* **268**, 339 (1991). doi:[10.1016/0370-2693\(91\)91587-L](https://doi.org/10.1016/0370-2693(91)91587-L)
21. A.C. Villari et al., Measurements of reaction cross sections for neutron-rich exotic nuclei by a new direct method. *Phys. Lett. B* **268**, 345 (1991). doi:[10.1016/0370-2693\(91\)91588-M](https://doi.org/10.1016/0370-2693(91)91588-M)
22. A. Ozawa, T. Suzuki, I. Tanihata, Nuclear size and related topics. *Nucl. Phys. A* **693**, 32 (2001). doi:[10.1016/S0375-9474\(01\)01152-6](https://doi.org/10.1016/S0375-9474(01)01152-6)
23. D.Q. Fang, Y.G. Ma et al., Systematic behavior of isospin effect in fragmentation reactions. *High Energy Phys. Nucl. Phys.* **31**, 1 (2007)
24. T. Brohm, K.H. Schmidt et al., Statistical abrasion of nucleons from realistic nuclear-matter distributions. *Nucl. Phys. A* **569**, 821 (1994). doi:[10.1016/0375-9474\(94\)90386-7](https://doi.org/10.1016/0375-9474(94)90386-7)

25. W.D. Myers, W.J. Swiatecki, Droplet-model theory of the neutron skin. Nucl. Phys. A **336**, 267 (1980). doi:[10.1016/0375-9474\(80\)90623-5](https://doi.org/10.1016/0375-9474(80)90623-5)
26. W.D. Myers, K.H. Schmidt, An update on droplet-model charge distributions. Nucl. Phys. A **410**, 61 (1983). doi:[10.1016/0375-9474\(83\)90401-3](https://doi.org/10.1016/0375-9474(83)90401-3)
27. L.V. Chulkov et al., Total charge-changing cross sections for neutron-rich light nuclei. Nucl. Phys. A **674**, 330 (2000). doi:[10.1016/S0375-9474\(00\)00168-8](https://doi.org/10.1016/S0375-9474(00)00168-8)
28. D.Q. Fang, W.Q. Shen et al., Isospin effect of fragmentation reactions induced by intermediate energy heavy ions and its disappearance. Phys. Rev. C **61**, 044610 (2000). doi:[10.1103/PhysRevC.61.044610](https://doi.org/10.1103/PhysRevC.61.044610)
29. T. Yamaguchi, M. Fukuda et al., Energy-dependent charge-changing cross sections and proton distribution of  $^{28}\text{Si}$ . Phys. Rev. C **82**, 014609 (2010). doi:[10.1103/PhysRevC.82.014609](https://doi.org/10.1103/PhysRevC.82.014609)
30. A. Bhagwat, Y.K. Gambhir, Microscopic investigations of mass and charge changing cross sections. Phys. Rev. C **69**, 014315 (2004). doi:[10.1103/PhysRevC.69.014315](https://doi.org/10.1103/PhysRevC.69.014315)
31. C. Zeitlin, A. Fukumura, S.B. Guetersloh et al., Fragmentation cross sections of  $^{28}\text{Si}$  at beam energies from 290A to 1200A MeV. Nucl. Phys. A **784**, 341–367 (2007). doi:[10.1016/j.nuclphysa.2006.10.088](https://doi.org/10.1016/j.nuclphysa.2006.10.088)
32. I. Angeli, K.P. Marinova, Table of experimental nuclear ground state charge radii: an update. At. Data Nucl. Data Tables **99**, 69 (2013). doi:[10.1016/j.adt.2011.12.006](https://doi.org/10.1016/j.adt.2011.12.006)